Physics of the Earth and Planetary Interiors 187 (2011) 353–363

Contents lists available at ScienceDirect

Physics of the Earth and Planetary Interiors

journal homepage: www.elsevier.com/locate/pepi

End-member models of boundary-modulated convective dynamos

Jonathan M. Aurnou [a,*], Julien Aubert [b]

[a] Department of Earth and Space Sciences, University of California, Los Angeles, 90095-1567, USA
[b] 2 Dynamiques des Fluides Géologiques, Institut de Physique du Globe de Paris, Université Paris-Diderot, PRES Sorbonne Paris Cité, INSU/CNRS UMR 7154, 1 Rue Jussieu, 75238 Paris Cedex 5, France

ARTICLE INFO

Article history:
Received 16 January 2011
Received in revised form 21 May 2011
Accepted 24 May 2011
Available online 7 June 2011
Edited by Keke Zhang

Keywords:
Planetary dynamos
Core–mantle interactions
Stratification
Geophysical fluid dynamics

ABSTRACT

Convective planetary dynamos depend upon secular cooling and internal radioactive decay for generating fluid motions within the core. Some planetary dynamo models also include heat flux variations along the core–mantle boundary (CMB) that modify the dynamo process. Here we study the effects of CMB heat flux variations in two sets of numerical dynamo models. In the first set, the possibility of dynamo action in a stably-stratified, Boussinesq, rotating spherical fluid shell is investigated. In these cases, lateral variations in CMB heat flux can drive significant zonal flows, but no dynamo action develops. In the second set of models, the fluid shell is neutrally-stratified. Dynamo action in these models is controlled by the pattern of CMB heat flux.

Our neutrally-stratified models are relevant for studying the limiting effects of strong boundary forcing acting atop a convectively well-mixed state. We study four neutrally-stratified dynamo cases with different spherical harmonic heat flux patterns imposed on the CMB: $Y10$, $Y11$, $Y20$ and $Y22$. These cases demonstrate that the fundamental symmetries of the dynamo field follow the spatial symmetries of the CMB heat flux pattern. Our results show that convective dynamos are not necessarily killed by boundary-driven thermal winds, a result of interest if Earth's core top is close to adiabatic. A strong $Y10$ forcing is likely to produce a dynamo with hemispherical magnetic field structure reminiscent of Mars surface magnetization. However, as boundary-modulated convective dynamos produce magnetic fields generally one order of magnitude weaker than homogeneous convective dynamos with an equivalent forcing amplitude, it seems unlikely that this process is at the origin of Mars' regions of strong crustal magnetization.

1. Introduction

In traditional models of the geodynamo (Christensen and Aubert, 2006; Wicht and Tilgner, 2010), a homogeneous heat loss to the mantle drives columnar convection in the Earth's liquid iron outer core, which continually converts the mechanical energy of the electrically-conducting fluid into magnetic field energy. In the mid- to high-latitudes, these models typically contain patches of magnetic flux below the outer boundary that consistently drift westward. However, asymmetries in the paleomagnetic and archeomagnetic records suggest that the geomagnetic field contains some features that remain fixed with respect to the overlying mantle (Gubbins and Kelly, 1993; Johnson et al., 2003). In attempting to incorporate such stationary features, models of rotating convection (Zhang and Gubbins, 1992, 1993, 1996; Gibbons and Gubbins, 2000; Gibbons et al., 2007; Davies et al., 2009) and dynamo action have included laterally-heterogeneous thermal features on the core–mantle boundary (CMB) (Glatzmaier et al., 1999; Olson and Christensen, 2002; Gubbins et al., 2007, 2011; Willis et al., 2007; Aubert et al., 2008; Sreenivasan, 2009). These heat flux variations can induce (i) boundary resonant, locked flows (Zhang and Gubbins, 1996), which typically arise very close to the onset of convection, and (ii) 'thermal wind' flows (Aurnou et al., 2003; Aubert, 2005), which describe axial shears in the velocity field that maintain geostrophic balance in the fluid (Vallis, 2006). Following Zhang and Gubbins (1992), we will use the terms 'boundary-driven' or 'boundary-modulated' when referring generally to flows generated by lateral variations in CMB heat flux.

In geodynamo models, boundary-modulated flows can modify the magnetic field (Olson and Christensen, 2002; Gubbins et al., 2007), sometimes even locking the field to the mantle, e.g. (Willis et al., 2007). However, it has also been shown that strong boundary-modulated flows, with velocities approaching those of the columnar motions, tend to overwhelm the convection. In this regime, dynamo action becomes weakened or is destroyed altogether, cf. (Olson and Christensen, 2002; Takahashi et al., 2008). These studies show that boundary-modulated flows can substantially alter the characteristics of a convection-driven dynamo.

There are planets that have magnetic fields, such as Mercury, Ganymede and possibly Io, where traditional convection-driven dynamo models may not apply, e.g. (Kerswell and Malkus, 1998;

* Corresponding author. Tel.: +1 310 825 2054; fax: +1 310 825 2779.
E-mail addresses: aurnou@ucla.edu (J.M. Aurnou), aubert@ipgp.fr (J. Aubert).

0031-9201/$ - see front matter © 2011 Elsevier B.V. All rights reserved.
doi:10.1016/j.pepi.2011.05.011

Christensen, 2006; Bland et al., 2008). For these bodies, it is possible that non-trivial heat flux variations exist on their CMBs that are capable of producing significant boundary-driven flows. On Mercury, for instance, mantle convection in a relatively thin shell geometry can induce a complex pattern of heat flux variations on the CMB (e.g. King, 2008). Boundary-driven flows are also likely to occur on planets in synchronous orbits, like the Galilean satellites, that undergo significant tidal flexing. This flexing produces a heat flux pattern that is a mix of $Y20$, $Y22$ and $Y44$ spherical harmonic components, whose relative strengths vary with planetary geometry and viscosity structure (Segatz et al., 1988; Tackley et al., 2001; Bland et al., 2008). Catastrophic impacts have also been proposed as a mechanism to produce a heterogeneous thermal field within a planet's deep interior (Stanley et al., 2008; Roberts et al., 2009).

It is plausible that boundary modulated flows are dynamically significant in the cores of planets with regionally-focused, massive volcanic provinces, such as the Tharsis region on Mars (Harder, 1998), the Procellarum KREEP terrane on the Moon (Stegman et al., 2003), or the Ontong-Java Plateau on Earth (Courtillot and Olson, 2007). The presence of these massive volcanic provinces suggests that, at some point in the planet's geologic history, a superplume developed on the CMB (Torsvik et al., 2006; Courtillot and Olson, 2007), capable of driving a strong spherical harmonic degree 1 CMB heat flux pattern that could generate a significant boundary-driven flow in the core (see also Zhong and Roberts, 2006; Stanley et al., 2008; Roberts et al., 2009). Downwelling flows in the lowermost mantle can generate significant CMB heat flux variations as well. Laboratory models of such systems estimate that heat flux variations can approach roughly 50% of the mean heat flux emerging from a planet's core (Gonnermann et al., 2004).

Thus, it is reasonable, first, to expect that boundary-driven flows develop in a wide range of planetary cores, and, second, to explore what effects such flows can have on planetary dynamo processes. In this study, we extend the kinematic models of Sarson (2003) and the geodynamo models of Sreenivasan (2009) by presenting the results of Boussinesq dynamo models driven by strong CMB heat flux variations.

2. Thermal winds and thermodynamic efficiencies

In this rapidly rotating system, a thermal wind response is typical when fluid density isosurfaces are misaligned from pressure isosurfaces (Vallis, 2006). Such a misalignment creates a baroclinic torque on the fluid and the vorticity equation becomes a balance, respectively, between Coriolis torque and this baroclinic term:

$$\frac{\partial \mathbf{u}}{\partial z} = -\frac{g}{2\rho\Omega r}(r\mathbf{e_r} \times \nabla\rho). \tag{1}$$

Here $\mathbf{u}$ is the velocity vector measured in the rotating frame, z is the coordinate along $\mathbf{e}_z$, g is gravitational acceleration, ρ is the fluid density, and Ω is the constant angular rotation rate of the shell along $\mathbf{e}_z$. Eq. (1) shows that horizontal gradients in fluid density in colatitude θ and azimuth φ are balanced by terms involving axial shears in the velocity field. Expanding (1) into component form yields

$$\frac{\partial u_\varphi}{\partial z} = -\frac{g}{2\rho\Omega r}\left(\frac{\partial \rho}{\partial \theta}\right); \tag{2}$$

$$\frac{\partial u_\theta}{\partial z} = +\frac{g}{2\rho\Omega r}\left(\frac{1}{\sin\theta}\frac{\partial \rho}{\partial \varphi}\right). \tag{3}$$

Thus, colatitudinal density gradients produce azimuthal shear flows, and azimuthal density gradients produce axially-varying meridional flows. The term 'thermal wind' derives from the assumption that the fluid's density varies primarily in proportion to temperature variations.

Thermal wind flows are driven by lateral density gradients and can exist even in stably-stratified fluid layers such as the Earth's atmosphere and oceans (Vallis, 2006). These flows seek to homogenize a laterally non-uniform temperature distribution of the overlying mantle. In contrast, thermal convective flows seek to homogenize radial temperature differences between the core and mantle.

Thermodynamic efficiency arguments (Lister, 2003 and references therein) show that lateral heat flux variations are orders of magnitude less efficient than radial heat fluxes in generating dynamo fields. For instance, the efficiency, ϵ, at which a given core–mantle boundary heat flux can be dissipated ohmically, has an upper bound defined by

$$\epsilon \leqslant \frac{T_{input} - T_{output}}{T_{rep}} \tag{4}$$

where T_{input} is the (absolute) temperature at which heat enters the system, T_{output} is the temperature at which heat enters the system, and T_{rep} is a temperature representative of the whole system.

For the geodynamo, we can take the temperature on the inner core boundary (ICB) as $T_{input} \sim 5000$ K and the temperature on the CMB as $T_{output} \sim 3000$ K. Taking the representative system temperature to be T_{CMB}, we then arrive at

$$\epsilon \leqslant \frac{T_{ICB} - T_{CMB}}{T_{CMB}} \sim \frac{5000 - 3000}{3000} = 2/3. \tag{5}$$

The actual efficiency for the present-day Earth is estimated to be about $\epsilon \approx 0.3$, a third of which comes from thermal convection and the rest from chemical convection (Lister, 2003).

In contrast, CMB heat flux variations alone produce a markedly different result. Using $\delta\rho = (\rho\,\alpha\,\delta\,T)$ where α is the thermal expansivity, Eq. (1) yields the scaling

$$\delta T \sim \frac{U\Omega}{\alpha g}. \tag{6}$$

Taking an upper bounding velocity scale of $U \sim 10^{-3}$ m/s and Earth core values for the other parameters (e.g. King et al., 2010), relationship (5) gives $\delta T \sim 10^{-3}$ K. This implies a CMB-driven thermodynamic dynamo efficiency of

$$\epsilon \leqslant \frac{U\Omega}{\alpha g T_{CMB}} \sim \frac{\delta T}{T_{CMB}} \sim \frac{10^{-3}}{3000} \sim 3 \times 10^{-7}. \tag{7}$$

Thus, we expect lateral heat flux variations on a planet's CMB will be capable of driving dynamos with roughly one-millionth the energetic efficiency of a comparable radial convective heat flux. Using the magnetic field scaling prediction from Christensen and Aubert (2006) gives that the ohmic dissipation, Φ_η, scales as the cube of the magnetic field strength, $\Phi_\eta \propto |B|^3$ (see also Aubert et al., 2009). This relationship, with (7), implies that lateral heat flux variations will be capable of generating dynamo fields that are roughly one-hundredth the intensity of fields produced by convection driven flows in terrestrial planets similar to Earth. Although it is not considered in further detail here, we note that our thermal wind scaling estimate for $|B|$ is not inconsistent with Mercury's weak magnetic field.

The efficiency arguments above show that relatively small temperature differences on the CMB should be able to drive only relatively weak planetary magnetic fields. It is much more difficult for boundary modulation to drive dynamo action in a stably-stratified fluid shell. Unless the stably-stratified system can undergo a large-scale baroclinic instability, as proposed in (Teed et al., 2010), any boundary-driven poloidal flows are likely to remain trapped near the boundary. For such boundary-trapped poloidal flows, the radial

length scale of motion is likely to be too small for dynamo action to develop.

3. Modeling approach

We numerically model fluid flow and magnetic induction subject to the Boussinesq and magnetohydrodynamic approximations (Gubbins and Roberts, 1987). Thus, we consider an incompressible, electrically conducting fluid in a spherical shell between inner and outer radii r_i and r_o. A spherical coordinate frame is adopted with radial, colatitudinal, and azimuthal unit vectors $\mathbf{e_r}, \mathbf{e}_\theta, \mathbf{e}_\varphi$, respectively. The spherical shell of fluid rotates about an axis $\mathbf{e}_z$ with constant angular velocity Ω, and is subject to a spherically symmetric gravitational acceleration $\mathbf{g} = -(g_o r/r_o)\mathbf{e}_r$, where g_o is gravity at the outer boundary. Flow is thermally-driven in these models by an outer boundary heat flux of form:

$$q = q_o + q_L(\theta, \phi), \tag{8}$$

where q_o is the mean heat flux and q_L is the root-mean-squared value of the laterally-varying heat flux. A fixed temperature boundary condition is employed on the inner boundary.

In the majority of cases presented here, we investigate neutrally-stratified fluid layers such that $q_o = 0$. The velocity field $\mathbf{u}$, the magnetic field $\mathbf{B}$, and the thermal perturbation field T are then solved for using the following non-dimensionalized Navier–Stokes, induction, and energy equations:

$$\frac{\partial \mathbf{u}}{\partial t} + \mathbf{u}\cdot\nabla\mathbf{u} + 2\mathbf{e}_z \times \mathbf{u} + \nabla P = Ra_L \frac{\mathbf{r}}{r_o} T + (\nabla \times \mathbf{B}) \times \mathbf{B} + E\nabla^2\mathbf{u} \tag{9}$$

$$\frac{\partial \mathbf{B}}{\partial t} = \nabla \times (\mathbf{u} \times \mathbf{B}) + \frac{E}{Pm}\nabla^2\mathbf{B} \tag{10}$$

$$\frac{\partial T}{\partial t} + \mathbf{u}\cdot\nabla T = \frac{E}{Pr}\nabla^2 T \tag{11}$$

$$\nabla\cdot\mathbf{u} = 0 \tag{12}$$

$$\nabla\cdot\mathbf{B} = 0 \tag{13}$$

These non-dimensional equations are obtained by scaling time with the inverse of the angular rotation rate Ω^{-1}; length with the spherical shell gap width $D = r_o - r_i$; velocity with ΩD; magnetic induction with $(\rho\mu)^{1/2}\Omega D$, where μ is the magnetic permeability of free space; temperature with $q_L/\rho C_p \Omega D$, and C_p is the specific heat of the fluid.

The dimensionless parameters involved in this study are the Ekman number $E = \nu/\Omega D^2$, where ν is the fluid viscosity; the Prandtl number $Pr = \nu/\kappa$, where κ is the thermal diffusivity; the magnetic Prandtl number $Pm = \nu/\eta$, where η is the magnetic diffusivity; and the Rayleigh number based only on the laterally-varying outer boundary heat flow $Ra_L = \alpha g_o q_L/\rho C_p \Omega^3 D^2$. The Rayleigh number can also be written as $Ra_L = F/\Omega^3 D^2$, where $F = \alpha g_o q_L/\rho C_p$ is the buoyancy flux (Aubert, 2005). The Ekman number, the Prandtl and magnetic Prandtl numbers, and the radius ratio are held fixed in this study with values of $E = 3\times10^{-4}, Pr = 1$, and $Pm = 2$. Lastly, the spherical shell radius ratio is also held fixed at $\chi = r_i/r_o = 0.35$.

The boundary conditions are of rigid type for the velocity field, and insulating for the magnetic field. Consistent with the definition of the Rayleigh number, the heat flux is fixed at the outer boundary. The temperature is fixed at the inner boundary. The numerical implementation MAGIC is used in this study (Wicht, 2002; Wicht and Tilgner, 2010). The spherical shell boundaries are rigid, non-slip, electrically insulating, and co-rotate at the fixed angular rate Ω. Hyperdiffusivities are not employed. For all the simulations, a Chebyshev polynomial expansion is used in the radial direction with 41 radial grid points. A spherical harmonic expansion is used in the lateral directions, containing harmonics up to maximum degree and order 64. We have carried out an additional, higher resolution calculation, using 65 radial grid points and spherical harmonics up to degree and order 85, which verifies our Y10 dynamo simulation results.

In some simulations, we also impose a laterally uniform heat flux that radially crosses the shell, with a value q_o at the outer boundary. In these cases, the temperature is non-dimensionalized with $q_o/\rho C_p \Omega D$, and the Rayleigh number appearing in (9) is now $Ra_Q^* = \alpha g_o q_o/\rho C_p \Omega^3 D^2$. The lateral Rayleigh number Ra_L does not appear in the controlling equations in these case but still controls the magnitude of the outer boundary imposed lateral heat flow heterogeneity.

In two of our models, we set $Ra_Q^* < 0$. These models are representative of a planetary core that is stably-stratified (i.e. subadiabatic) throughout. Strong thermal wind-style flows develop in these models, with no convection occurring anywhere in the shell. In the five other models presented, we set $Ra_Q^* = 0$. These models are representative of a planetary core that is neutrally stratified (i.e. adiabatic) throughout. This is the case because, in the Boussinesq limit, the base state is that of a well-mixed fluid. By setting $Ra_L \neq 0$, the large-scale dynamics are modulated by the lateral buoyancy forcing we apply at the CMB. In regions of the shell where the CMB heat flux is directed outwards from the core, our $Ra_Q^* = 0$ models are dominated by strong convective flows. In the parts of the shell where the CMB heat flux is directed into the core, the fluid is stably-stratified and thermal wind-style flows tend to dominate.

Fig. 1 is a schematic of the parameter space investigated here. Our stably-stratified models should be thought to exist in Regime I: (i) below the horizontal line demarcating $Ra_Q^* = 0$ and (ii) where the dynamical effects of lateral buoyancy forcing will be significant. Our neutrally-stratified models can be thought to map to Regime III: (i) just above the horizontal line where a background convection field produces well-mixed fluid throughout the shell, but (ii) far to the right of the long-dashed vertical line where the lateral buoyancy effects will be significant.

For example, if the fluid in the vicinity of Earth's CMB is nearly adiabatic than mantle-driven thermal heterogeneity can strongly affect the dynamics (i.e. $Ra_L \gtrsim Ra_Q^*$(CMB); Regime III), e.g. (Sumita

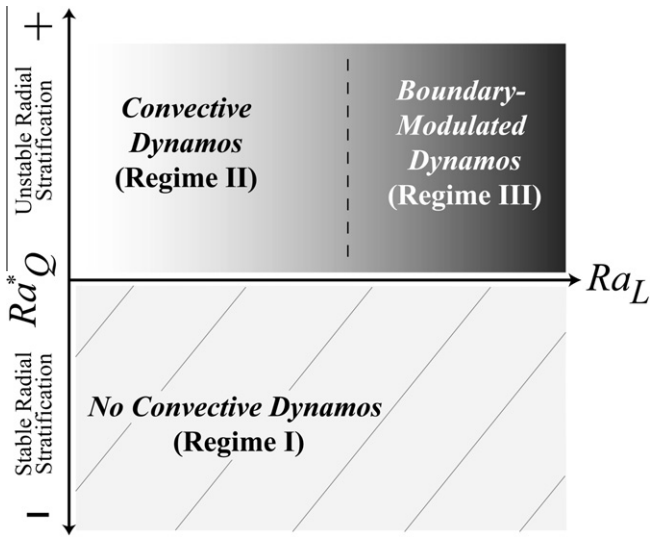

Fig. 1. Schematic diagram of dynamo generation regimes in a system with varying Ra_L and Ra_Q^* values and fixed E, Pr, Pm, r_i/r_o and outer boundary heat flux pattern. Regime I: Stably-stratified fluid layers in which it is difficult to develop dynamo action. Regime II: Convective dynamo action. We assume in this schematic that the critical Rayleigh number for the onset of convection and dynamo action occurs very near $Ra_Q^* \sim 0$. Regime III: Dynamo action in a well-mixed fluid layer subject to flows driven by laterally variations of CMB heat flux (i.e. boundary modulation).

Table 1
Numerical modeling results all for fixed values of Ekman number $E = 3 \times 10^{-4}$, Prandtl number $Pr = 1$, magnetic Prandtl number $Pm = 2$, and radius ratio $\chi = 0.35$. The first column gives the radial stratification of the model, controlled by the Rayleigh number Ra_Q^*. The second column gives heat flux pattern on the model's outer boundary. The third column gives the lateral Rayleigh number, Ra_L. The fourth column gives Ra_L normalized by the Rayleigh number for the onset of rotating convection, $(Ra_Q^*)_{crit} = 5.47 \times 10^{-6}$ (Christensen and Aubert, 2006). The fifth column gives the magnetic Reynolds number, Re_M. The sixth column provides the strength of the rms magnetic field in the shell normalized by the convective magnetic field scaling from Christensen and Aubert (2006). The seventh column gives the Elsasser number, Λ. The eighth column the average time period between polarity reversals in magnetic diffusion time-scale units, r_o^2/η. Non-reversing cases are labeled 'NR.'

Ra_Q^*	Pattern	Ra_L	$Ra_L/(Ra_Q^*)_{crit}$	Re_M	B_{rms}/B_{CA06}	Λ	Reversal period
-1.80×10^{-3}	*Y*20	1.80×10^{-4}	32.5	131	no dynamo	0	–
-1.80×10^{-3}	*Y*22	1.80×10^{-4}	32.5	9.7	no dynamo	0	–
0	*Y*10	2.70×10^{-4}	49.4	310	3.0×10^{-2}	0.025	~0.17
0	*Y*11	7.64×10^{-5}	14.0	92	3.2×10^{-2}	0.012	NR
0	*Y*20	6.75×10^{-6}	1.2	36	no dynamo	0	–
0	*Y*20	3.38×10^{-5}	6.2	132	1.5×10^{-1}	0.16	NR
0	*Y*22	1.91×10^{-4}	34.9	123	1.3×10^{-1}	0.37	NR

and Olson, 2002; Aubert et al., 2008; Gubbins et al., 2011). In contrast, if the superadiabatic CMB heat flow is dominant, the resulting flows will not be strongly affected by CMB heterogeneity and our models will not apply (i.e. $Ra_L < Ra_Q^*$(CMB); Regime II). Similarly, if Io's core is well-mixed by tidal instability, e.g. (Kerswell and Malkus, 1998; Cébron et al., 2010), our Regime III models may represent the effects of strong lateral heterogeneity of the CMB thermal field. Should Io's core be stably-stratified, e.g. (Khurana et al., 2011), then our Regime I models may better apply.

The parameters of the two stably-stratified and the five neutrally-stratified simulations are given in Table 1. In order to facilitate comparison with related dynamo models, we provide the following output parameters: the magnetic Reynolds number defined as $Re_M = U_{rms}/\Omega D$ where U_{rms} is the root-mean-squared velocity in the shell and B_{rms}/B_{CA06}, which is the root-mean squared magnetic field amplitude in the shell normalized by the scaling prediction from (Christensen and Aubert, 2006), $B_{CA06} = \sqrt{\rho\mu}(FD)^{1/3}$. In addition, the Elsasser number $\Lambda = B_{rms}^2/(\lambda\mu\rho\Omega)$ and the dipole reversal rate are also reported.

4. Results

4.1. Stably-stratified non-dynamo simulations

We have carried out stably-stratified simulations for two different CMB heat flux patterns, *Y*20 and *Y*22 (see Table 1). In these two cases, stable stratifications are employed ($Ra_Q^* = -1.80 \times 10^{-3}$) as well as CMB boundary modulation ($Ra_L = -1.80 \times 10^{-4}$). Fig. 2 shows the results of the *Y*20 stably-stratified simulation. This *Y*20 pattern of heat flux simulates the effects of axisymmetric, latitudinal thermal variations on the model's CMB; heat is driven out of the core at the poles and into the core in the equatorial region (Figs. 2a and 3a). The resulting thermal wind consists of axisymmetric azimuthal (i.e. zonal) flows, as predicted by Eq. (2). (In contrast to the neutrally-stratified *Y*20 cases presented in Section 4.2.1, the thermal wind is prograde here because of the negative Ra_Q^* that replaces Ra_L in (9).) These azimuthal flows also induce poloidal flows via Ekman pumping through the viscous boundary layers (Vallis, 2006). Since these poloidal flows scale as $E^{1/2}$ of the typical flow velocity, they are only $\approx 1\%$ the strength of the azimuthal thermal wind. Furthermore, these poloidal flows do not penetrate into the stably-stratified fluid interior. Instead, they remain trapped close to the outer boundary, as can be inferred from the very low magnetic Reynolds number reached in a *Y*22 simulation (see Table 1), which has no axisymmetric heat flux variation. Thus, the weak poloidal flow prevents dynamo action, even though the *Y*20 case's toroidal flow is strong.

Motivated by Teed et al. (2010), we had hoped to test explicitly whether dynamo action can arise in a stably-stratified fluid layer that undergoes a three-dimensional, baroclinic instability. Scaling estimates of the Eady growth rate (Vallis, 2006) imply that baroclinic instabilities should be possible in the *Y*20 case. However, no such instabilities develop from this model's zonal shears (Fig. 2c). These models are probably too viscous for baroclinic instabilities to develop; i.e. the Reynolds numbers in the *Y*20 case, $Re = Re_M/Pm \approx 65$, is rather modest.

4.2. Neutrally-stratified dynamo simulations

We have carried out neutrally-stratified simulations for four different CMB heat flux patterns. We find that the onset of buoyancy-modulated dynamo action and the shapes of the dynamo

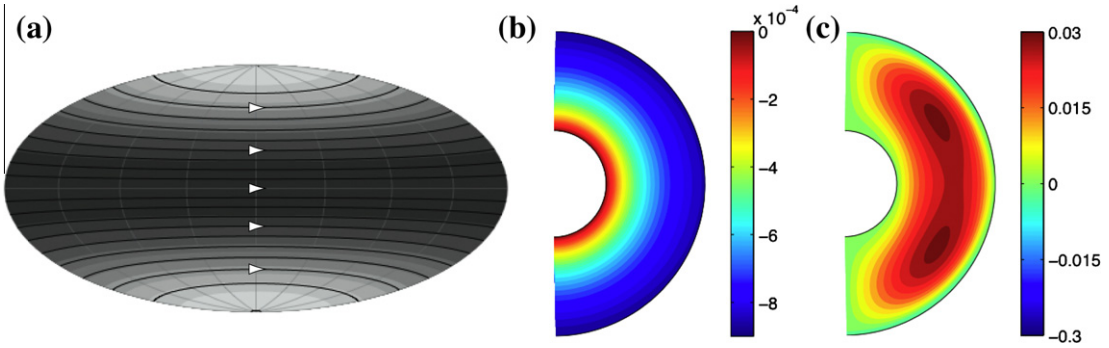

Fig. 2. Snapshot images of the *Y*20 Regime I non-dynamo case ($Ra_L = 1.80 \times 10^{-4}$; $Ra_Q^* = -1.80 \times 10^{-3}$). (a) Greyscale contours show the pattern of heat flux on the CMB. Light (dark) shades denote radially outwards (inwards) CMB heat flow. Line contours show streamlines of the flow field just below the Ekman layer (on $r = 0.993\ r_o$, similar to Aubert et al. (2007). Meridional slices showing color contours of (b) non-dimensional temperature variations and (c) azimuthal velocities in non-dimensional Rossby number units. Red (blue) contours represent warmer (cooler) fluid and prograde (retrograde) velocities, respectively. (For interpretation of the references in colour in this figure legend, the reader is referred to the web version of this article.)

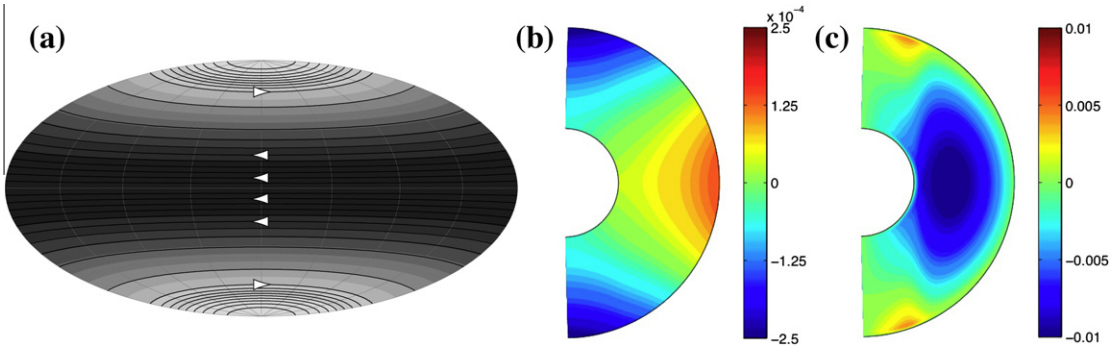

Fig. 3. Snapshot images of the *Y*20 Regime III non-dynamo case ($Ra_L = 6.75 \times 10^{-6}$; $Ra_Q^* = 0$). See Fig. 2 caption for detailed panel descriptions.

generated fields are both functions of the imposed heat flux pattern.

4.2.1. Axisymmetric heat flux patterns

Fig. 3 shows the results of a neutrally-stratified case ($Ra_Q^* = 0$) with a relatively weak *Y*20 CMB heat flux, corresponding to $Ra_L = 6.75 \times 10^{-6}$. This calculation does not produce dynamo action for two likely reasons. First, it is difficult, although not theoretically impossible, to generate self-sustaining dynamo action by axisymmetric motions (Gubbins and Roberts, 1987), similar to the stably-stratified *Y*20 case. Second, the thermal wind flow is relatively weak in this case. For this case, the magnetic Reynolds number, which estimates magnetic field generation relative to diffusion, has a value of 36. This value lies just below the estimated critical value $Re_M \sim 40$ for dynamo action in the convection-driven dynamo simulations of Christensen and Aubert (2006). Thus, the axisymmetric velocity field, as well as its low intensity, both disfavor dynamo action.

Fig. 4 shows the results of a *Y*20 case with $Ra_L = 3.38 \times 10^{-5}$. In this more strongly-forced case, the flow becomes unstable at mid- to high latitudes. This instability produces non-axisymmetric, three-dimensional fluid motions, which are capable of supporting dynamo action. We argue that the high latitude fluid becomes convectively unstable since the local surface cooling produces a situation where cold fluid overlies warmer deep fluid. This high latitude convection effectively cools the fluid region primarily within the right axial 'tangent cylinder' that circumscribes the inner core equator. Cooling of the tangent cylinder fluid drives further thermal winds that may then become baroclinically unstable, e.g. (Aurnou et al., 2003). Irrespective of the specific instability mechanisms, the resulting flow is capable of generating a self-sustaining magnetic field, with dynamo generation occurs predominantly at higher latitudes. The magnetic field at the CMB is closely aligned with the rotation axis. Little magnetic flux enters or exits the core except in strong polar flux patches (Figs. 2b and 3a). Using the magnetic field intensity scaling proposed in Christensen and Aubert (2006), we find that the field produced by this *Y*20 Boussinesq dynamo is approximately an order of magnitude weaker than that of a comparable convectively-driven dynamo model (Table 1).

Fig. 5 shows the results from a dynamo case with a *Y*10 CMB heat flux pattern and $Ra_L = 2.70 \times 10^{-4}$. Similar to the previous *Y*20 cases, the *Y*10 heat flux pattern is axisymmetric. However, the *Y*10 pattern is equatorially antisymmetric. This equatorial asymmetry generates significantly different flow and magnetic field morphologies in comparison to the *Y*20 case. The streamlines in Fig. 5a show that only the flow in the northern hemisphere (outward CMB heat flux) becomes unstable to three-dimensional motions, cf. (Holme and Ingersoll, 1994). In the southern hemisphere (inward CMB heat flux), the flow is axisymmetric and laminar. The Ekman pumping in this case produces a relatively strong large-scale, laminar poloidal flow, with a north to south jet below the outer boundary and a broad recirculation occurring throughout the region exterior to the tangent cylinder (Fig. 5c). This recirculation advects the southern retrograde azimuthal flow northward across the equator. In addition, it compresses the region of prograde azimuthal flow in the northern hemisphere.

This case produces a quasi-periodically reversing dynamo, which has an external magnetic field that is hemispherical in nature. The high latitude three-dimensional flow in the northern hemisphere produces intense, small-scale poloidal field patches, predominantly inside the tangent cylinder. In order to create such a localized CMB magnetic field, the power spectrum for this case must be rather broad band (Fig. 5d). The retrograde azimuthal flows in the southern hemisphere generate strong toroidal fields in this part of the shell (Fig. 5c). Opposing gradients in the retrograde azimuthal flow (i.e. $\partial u_\varphi / \partial s < 0$ just outside the tangent cylinder and $\partial u_\varphi / \partial z > 0$ in the vicinity of the equatorial plane) generate two large bundles of oppositely signed toroidal field. The northern hemisphere poloidal field in this case is qualitatively similar to the polar fields in the *Y*20 dynamo case, however, a significantly stronger buoyancy forcing is needed in the *Y*10 case to create an unstable flow and, subsequently, a self-sustaining dynamo.

4.2.2. Non-axisymmetric heat flux patterns

In order to incorporate the effects of longitudinal variations in CMB heat flux, we have conducted two additional boundary-modulated dynamo simulations that, respectively, make use of *Y*11 and *Y*22 spherical harmonic outer boundary heat flux patterns. The *Y*11 case has heat leaving the eastern hemisphere of the core and entering the western hemisphere (Fig. 6a), simulating the CMB heat flux pattern produced by an equatorial mantle superplume. The *Y*22 case has heat leaving the core along two antipodal longitudinal bands and entering the core in the two neighboring longitudinal bands (Fig. 7a). This pattern simulates one of the dominant CMB heat flux components caused by tidal flexing of the silicate mantle (or ice shell) of a body in a synchronous elliptical orbit (Tackley et al., 2001; Segatz et al., 1988).

In both these cases, the flow field contains azimuthal shear flows due to the latitudinal heat flux variations (Eq. (2)) and upwelling/downwelling flows due to the longitudinal gradients in heat flux (Eq. (3)). In particular, downwellings are located on the retrograde side of warm regions and upwellings are located on the prograde side of warm regions, e.g. (Gibbons and Gubbins, 2000; Sarson, 2003; Sreenivasan, 2009).

From the alternating signs of this sectoral heat flux pattern, one might expect that there would be sectorally-localized azimuthal thermal winds, which would sum to produce no mean axisymmetric azimuthal flow: $\oint u_\phi(r, \theta, \phi) d\phi = 0$. However, the results shown in Figs. 6c and 7c demonstrate that mean azimuthal retrograde thermal wind flows develop in the region outside the tangent

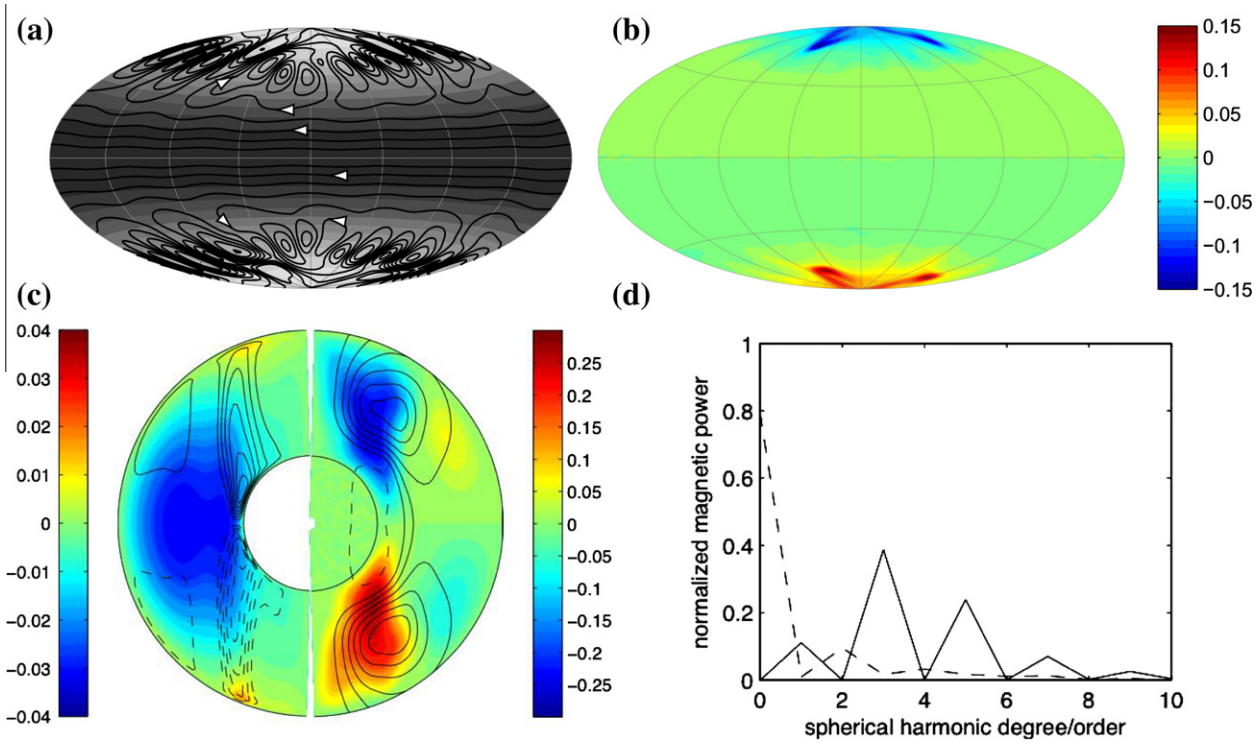

Fig. 4. Snapshot images of the *Y*20 Regime III dynamo case. (a) Greyscale shading show the pattern of heat flux on the CMB. Light (dark) shading indicates radially outwards (inwards) CMB heat flow. Line contours show streamlines of the flow field just below the Ekman layer (on $r = 0.993r_o$, similar to Aubert et al. (2007). (b) Radial magnetic field on the outer boundary. Field intensity is normalized using the B_{CA06} scaling for convection-driven dynamos from Christensen and Aubert (2006) (see text). (c) Meridional slices showing color contours of azimuthally-averaged azimuthal velocity (in Rossby number units, blue is retrograde) (left) and toroidal magnetic field (right, blue is retrograde). Line contours show azimuthally-averaged poloidal velocity (left) and poloidal magnetic field (right). (d) Magnetic power spectrum on the CMB normalized so that the total energy is unity. Solid (dashed) line shows power as a function of spherical harmonic degree, l (order, m). (For interpretation of the references in colour in this figure legend, the reader is referred to the web version of this article.)

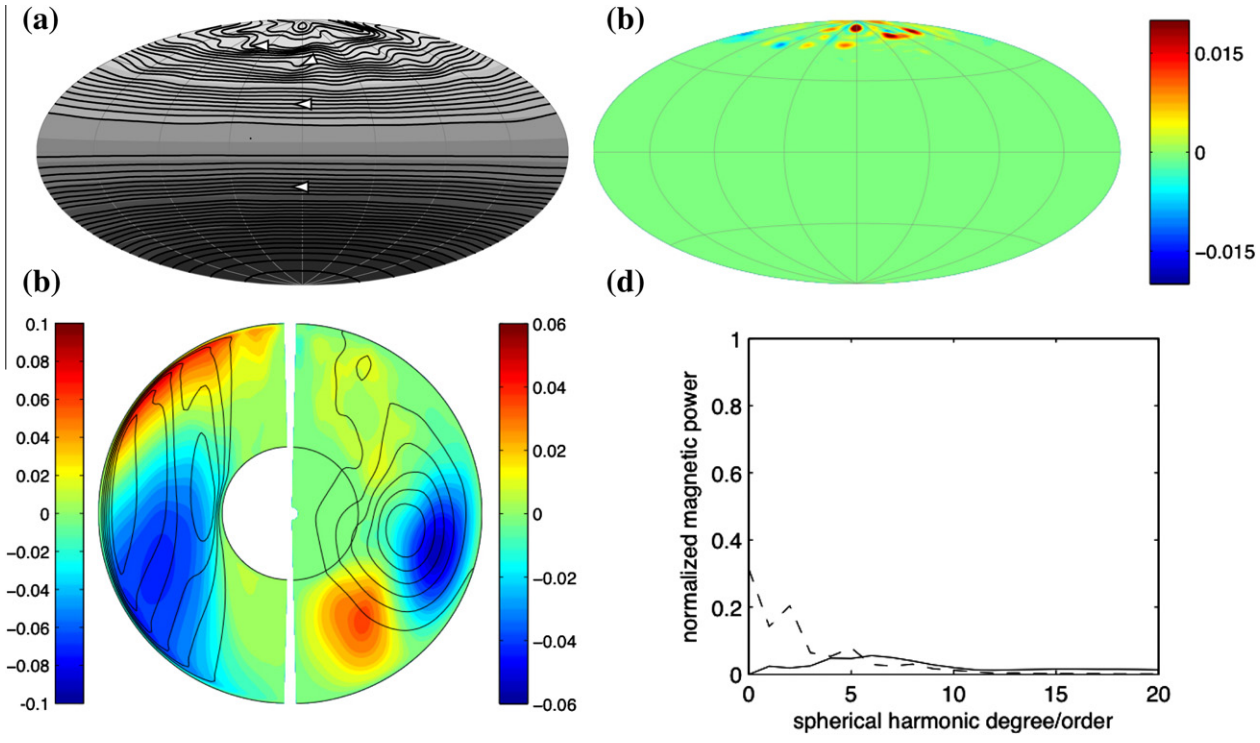

Fig. 5. Snapshot images of the *Y*10 Regime III dynamo case. See Fig. 4 caption for detailed panel descriptions.

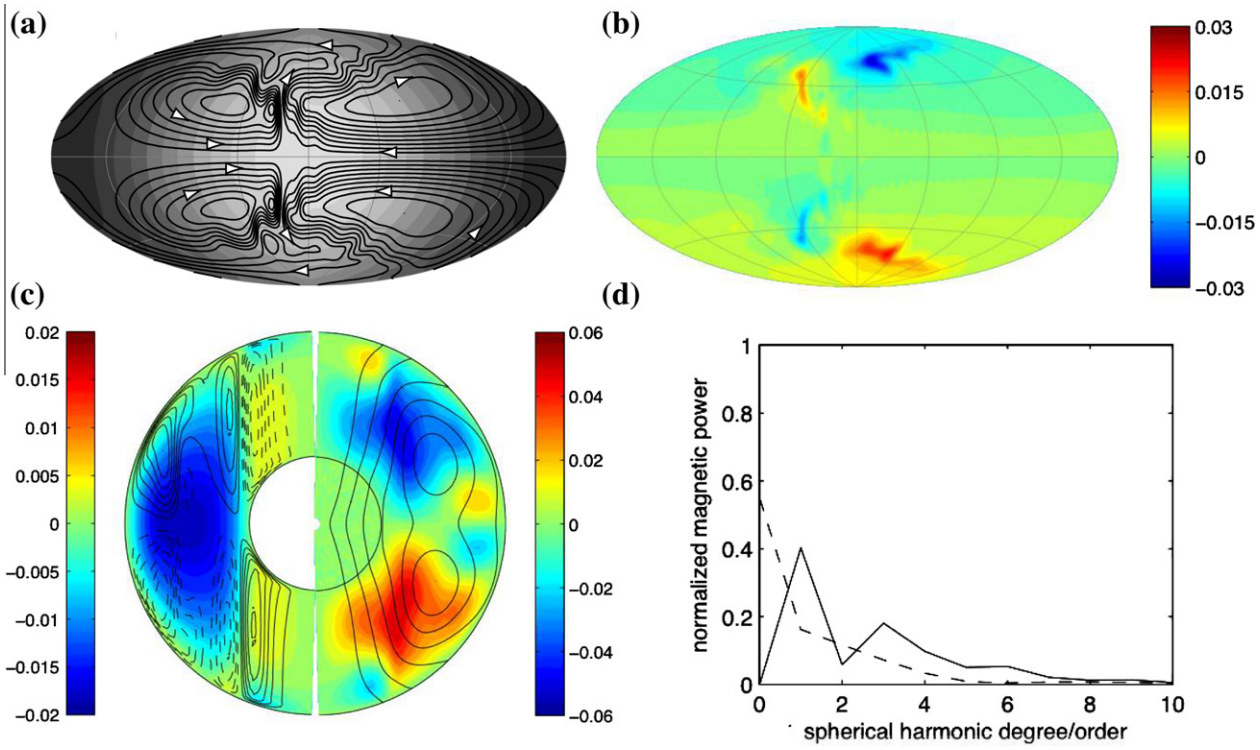

Fig. 6. Snapshot images of the *Y*11 Regime III dynamo case. See Fig. 4 caption for detailed panel descriptions.

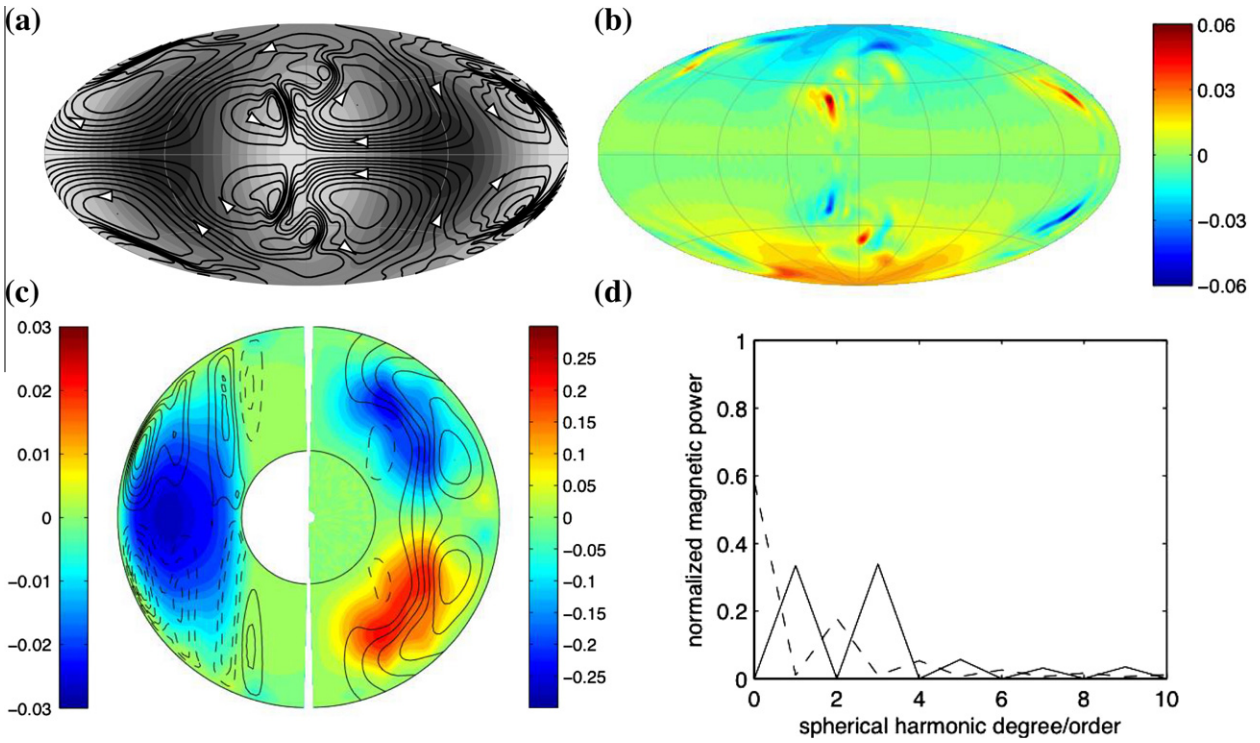

Fig. 7. Snapshot images of the *Y*22 Regime III dynamo case. See Fig. 4 caption for detailed panel descriptions.

cylinder. These modest axisymmetric thermal wind fields are similar in morphology to those that develop in the *Y*20 dynamo case (Fig. 4c). They develop because nonlinear advection of the temperature field by the sectoral thermal wind flows sets up a *Y*20 thermal field just below the outer boundary. In sectors with outward CMB heat flux, longitudinal thermal wind flows advect cold fluid towards the poles; in sectors with inward CMB heat flux, longitudinal thermal wind flows advect cold fluid towards the equator (Fig. 7a). The thermal advection by these flows induces a *Y*20 temperature field in which the polar regions are slightly cooler and the equatorial region is slightly warmer. In both these cases, this induced *Y*20 temperature field drives the retrograde mean azimuthal

thermal wind flows. This thermal advection mechanism differs fundamentally from the angular momentum advection mechanism put forth to explain the prograde equatorial jets inferred to exist in the atmospheres of tidally-locked hot Jupiters, cf. (Dobbs-Dixon and Lin, 2008).

Poloidal magnetic field generation occurs farther from the rotation axis in these non-axisymmetric heat flux cases (Figs. 6 b,c and 7b,c) than in comparable axisymmetric cases (Figs. 4b,c and 5b,c). In the outer region of the shell, large-scale shears in the azimuthal flow produce the toroidal magnetic fields. Localized radial flows, arising in the mid-latitudes where large azimuthal and longitudinal gradients in CMB heat flux exist, act on this toroidal field, twisting it into strong normal and reverse polarity flux spots. The location of the reverse polarity flux patches is controlled by the heat flux pattern on the CMB. This behavior differs from convection driven models ($Ra_L \ll Ra_Q^*$), where such patches tend to develop near the equator and in the vicinity of the tangent cylinder, e.g. (Wicht and Tilgner, 2010).

5. Discussion

5.1. Dynamo mechanisms

The magnetic field morphologies generated by our neutrally-stratified boundary-modulated dynamos ($Ra_L > 0$; $Ra_Q^* = 0$; Regime III) differ from those that occur in convection-driven dynamo models ($Ra_L \ll Ra_Q^*$), which often feature axial, dipolar fields (e.g. Wicht and Tilgner, 2010). Three-dimensional magnetic field line renderings (Aubert et al., 2008) of these dynamos (Fig. 8) and CMB power spectra (Figs. 4d, 5, 6, and 7d) show that the individual heat flux patterns lead to magnetic field morphologies that significantly differ from one another as well. The $Y20$ dynamo case is dominated by the axisymmetric octopole ($l = 3$) term. The $Y10$ case has a localized, complex CMB field with magnetic field energy spread out over spectral space. The $Y11$ case contains significant energy in its axial dipole ($l = 1$) and equatorial dipole ($m = 1$) components. The $Y22$ case has comparable axial dipole and octupole

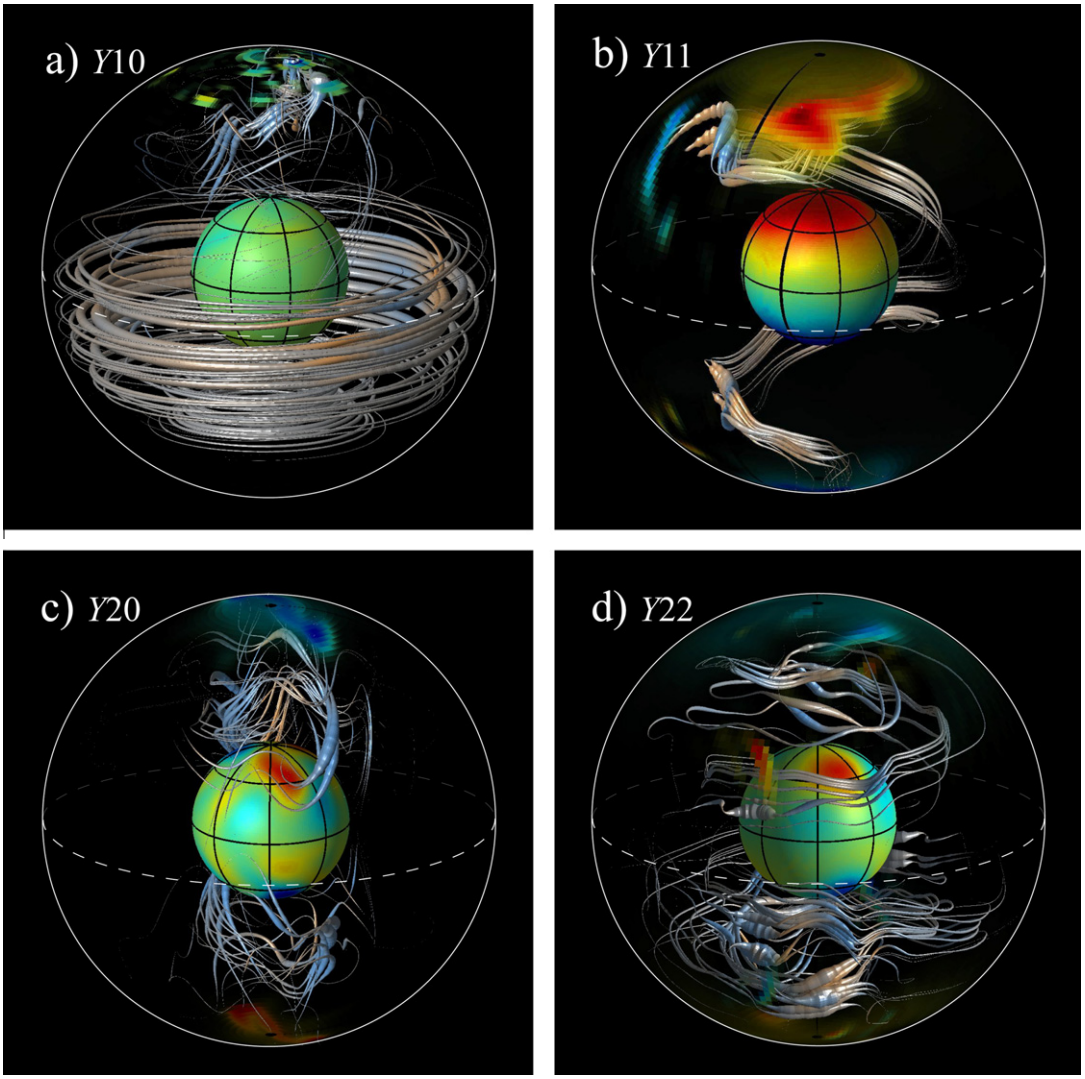

Fig. 8. Three-dimensional magnetic field line renderings for snapshots of the (a) $Y10$, (b) $Y11$, (c) $Y20$ and (d) $Y22$ Regime III dynamo cases, viewed from 15° above the equator. The magnetic field line thickness is rendered in proportion to local magnetic energy. An outer boundary great circle (solid line) and the equator (dashed line) are drawn in white. The inner (ICB) and outer (CMB) boundaries of the model are color-coded with the radial magnetic field (red patches denote outwardly oriented fields, the color coding is the same as on the hammer projections of previous figures, with ICB magnetic fields divided by 2. In addition, the outer boundary is made selectively transparent, with a transparency level that is inversely proportional to the local radial magnetic field intensity. Field lines are also color-coded in order to indicate the $\mathbf{e}_z$-parallel (red) and antiparallel (blue) directions. A detailed description of this rendering algorithm is given in Aubert et al. (2008). (For interpretation of the references in colour in this figure legend, the reader is referred to the web version of this article.)

terms, as well as a strong equatorial quadrupole ($m = 2$) term, in good agreement with Sreenivasan (2009).

5.1.1. Axisymmetric heat flux patterns

The first-order variation in the magnetic field structures shown in Fig. 8 implies that the dynamo mechanisms differ between the individual heat flux patterns. In the cases driven by axisymmetric heat flux patterns ($Y10$ and $Y20$), dynamo action has not been found to occur until the thermal wind becomes unstable to convective, and possibly baroclinic, instabilities. These three-dimensional (3D) instabilities generate intense small-scale poloidal fields. The instabilities develop in the vicinity of the tangent cylinder in both cases. In addition, the flow inside the tangent cylinder appears to contain large-scale axial thermal wind shears that create macroscopic poloidal and toroidal fields. Thus, the equatorially symmetric $Y20$ case produces dynamo action almost exclusively within the tangent cylinder.

In contrast, the equatorially anti-symmetric $Y10$ case generates a weak external field only in the northern hemisphere. In the southern hemisphere, large-scale ω-effects generate strong, quasi-periodically reversing toroidal fields. The poloidal fields, which are strongest in the southern hemisphere, are likely generated by a macroscopic α-effect controlled by the large-scale poloidal recirculation that is driven by Ekman pumping. This $Y10$ case, with its frequent reversals, appears to be a novel form of an $\alpha\omega$ dynamo wave solution. Grote and Busse (2000) and Busse and Simitev (2006) find hemispherical dynamos in models with mechanically stress-free, fixed heat flux boundary conditions. In these models, the internal and external field are both strongest in one hemisphere. In contrast, the region of expelled external field remains fixed in the northern hemisphere in our $Y10$ model, whereas the strong internal field remains fixed in the southern hemisphere.

The hemispherical Martian dynamo model of Stanley et al. (2008), driven by convection in conjunction with thermal wind flow ($Ra_L \sim Ra_Q^* > 0$), features a hemispherically locked external field similar to our $Y10$ case. This suggests that there is a broad $Ra_L - Ra^*Q$ parameter space that can produce hemispherically-locked dynamo fields. However, a significant difference occurs between our $Y10$ dynamo model and that of Stanley et al. (2008): the magnetic field in Stanley et al.'s model is non-reversing, whereas our $Y10$ model's magnetic field undergoes relatively frequent polarity reversals. The $Y10$ model reverses 6 times in 1 magnetic diffusion time r_o^2/η. If we assume a core radius of $r_o = 1700$ km, similar to that of Mars, one magnetic diffusion time is approximately 10^5 years and the $Y10$ model would reverse approximately every 15,000 years. This difference in reversal behavior is probably due to the choice of mechanical boundary conditions. The non-slip boundary conditions in our $Y10$ model drive a large-scale poloidal recirculation via pumping through the Ekman boundary layer. In contrast, no large-scale poloidal flow appears to exist in the Stanley et al. model, which employs stress-free boundary conditions. Furthermore, if our $Y10$ case is an $\alpha\omega$ dynamo wave solution, it is one of the only such solutions to develop specifically because of its non-slip boundary conditions.

5.1.2. Non-axisymmetric heat flux patterns

Dynamo action is produced by a similar mechanism in the $Y11$ and $Y22$ cases, which are both driven by non-axisymmetric, equatorially symmetric CMB heat flux patterns. In these cases, poloidal and toroidal magnetic fields are generated by thermal wind shears occurring outside the tangent cylinder. Locations of strong radial flow convert toroidal field into poloidal field in the regions of strong longitudinal thermal variations exist. The latitudinal thermal variations create sectoral azimuthal shears that stretch poloidal fields into toroidal fields. Furthermore, the axisymmetric zonal flows induce a significant component of the toroidal field. Thus, these cases appear to be macroscopic $\alpha^2\omega$ dynamos, qualitatively similar to the high E convective dynamo cases described in Olson et al. (1999) and Aubert et al. (2008). In these convective dynamo models, the dynamo mechanism is macroscopic in scale because the overly strong viscous effects in these models favor the formation of large-scale convection structures. However, it is not clear whether such structures pertain to actual planetary settings. In contrast, the large-scale structure of thermal wind flow does not depend on the fluid viscosity, and is dictated by the CMB thermal field. It is therefore likely that such thermal wind flows could pertain to planetary conditions, e.g. (Aubert et al., 2008). This behavior also accounts for the good agreement between our $Y22$ dynamo results, the comparable model of Sreenivasan (2009), and the $Y22$ kinematic dynamo model shown in Fig. 5 of Sarson (2003).

5.2. Implications

Boundary-modulated flows can act to either support or destroy dynamo action in a given planet's core. For instance, Olson and Christensen (2002) proposed that overly strong CMB heat flux variations will tend to drive thermal wind flows that destroy convection-driven dynamo action. Our present models show that this is not necessarily the case: for a variety of heat flux patterns, dynamo action is recovered in the limit of dominant heterogeneous boundary forcing ($Ra_L/Ra_Q^* \to \infty$). Our results are also in qualitative agreement with the dynamo modeling studies of Sreenivasan (2009) and Takahashi et al. (2008). For example, in Takahashi et al. (2008), they show that strong $Y22$ thermal winds are deleterious to convection-driven dynamo action at relatively high Ekman number values E (low rotation rates), but that the same CMB forcing enhances convection-driven dynamo action as the Ekman number E is decreased towards more realistic values (i.e. higher rotation rates).

The snapshot of the $Y10$ thermal wind dynamo model shown in Fig. 5b reveals a complex CMB magnetic field that is localized in the northern hemisphere, where the heat flux is directed outward. This magnetic field is qualitatively similar to the observed crustal field of Mars. Fig. 9 shows this field upward continued from the CMB to the surface of a 3400 km radius planet, assuming a 1700 km radius core. The surface field has a smooth spatial structure and is roughly an order of magnitude stronger in the northern hemisphere than in the southern hemisphere. The maximum amplitude of the surface field, B_{max}, is roughly three orders of magnitude weaker than a comparable convective dynamo surface magnetic field, such that $B_{max} \sim 10^{-4} B_{CA06}$. Taking a peak Noachian CMB heat flux of $q_o \sim 100$ mW/m^2 from Elkins-Tanton et al. (2005), we estimate that $B_{max} \sim 80$ nT. This instantaneous surface field intensity estimate is approximately two orders of magnitude too weak to account for the strong magnetizations inferred for the martian crustal materials (e.g. Brachfeld and Hammer, 2006).

We have time-averaged the $Y10$ model's magnetic field for just over one magnetic diffusion time scale, r_o^2/η. Assuming a 1700 km

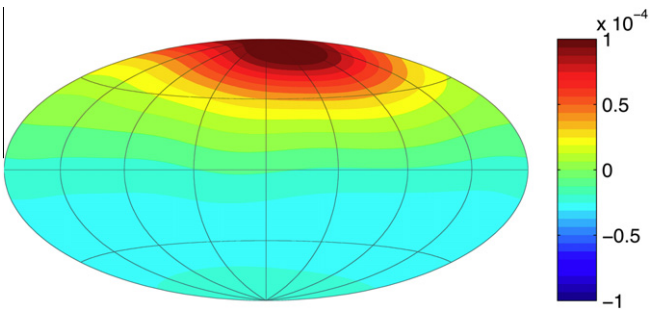

Fig. 9. $Y10$ dynamo field snapshot extrapolated to the surface of a Mars-like planet having a surface radius of 3400 km and a CMB radius of 1700 km.

radius martian core, this time scale corresponds to $\tau_\eta \simeq 10^5$ years. The magnetic field reverses six times over this time-averaging window, giving a characteristic polarity epoch time scale of $\tau_{rev} \simeq 15,000$ year. These relatively rapid reversals generate a time-averaged rms surface magnetic field that is another order of magnitude weaker than the surface field in Fig. 9, so that the estimated time-averaged $B_{max} \sim 10$ nT. It must be noted, though, that the scaling method for these estimates, borrowed from the convection simulations of Christensen and Aubert (2006) ($Ra_L = 0$; $Ra_Q^* > 0$), need not be accurate for our buoyancy-modulated dynamos ($Ra_L > 0$; $Ra_Q^* = 0$).

Our *Y*10 model's surface field does not seem capable of explaining other aspects of the martian observations, which are independent of the absolute intensity of the magnetic field. The hemispherical variation of the model's surface field intensity – by approximately one order of magnitude – is significantly less than the spatial variations observed on Mars (e.g. Purucker et al., 2000; Nimmo et al., 2008). Furthermore, the relatively frequent polarity reversals in our model would not leave a strong imprint on a thick layer of crustal material. Nimmo (2000) estimated that a 40–60 km thick layer of crust needs to be highly magnetized to explain the strength of the martian crustal anomolies. For instance, during our model's typical 15,000 year polarity epoch, a $\delta z \sim 2$ km of cooling crust can become magnetized, assuming the simple scaling $\delta z \sim \sqrt{\pi^2 \kappa \tau_{rev}}$ with $\kappa \simeq 10^{-6}$ m^2/s. Stacking many such 2 km thick layers of opposing magnetization will produce a weak external signal, unlike the martian observations. However, since the Ekman number is held fixed in this study at $E = 3 \times 10^{-4}$, it is not possible to determine how the *Y*10 model's reversal frequency changes as the Ekman number is lowered towards more realistic planetary values (e.g. $E \lesssim 10^{-10}$).

6. Summary

In this study, we have investigated Boussinesq models of planetary dynamo generation driven via a laterally-varying heat flux on the spherical shell's outer boundary.

In the stably-stratified cases (Regime I) performed here, flows driven by the laterally-varying CMB heat flux (i) remain baroclinically stable and (ii) never penetrate to significant depth within the fluid layer. Subsequently, dynamo action does not develop.

In neutrally-stratified cases (Regime III), the models represent the limit of strong heterogeneous boundary forcing acting on a well-mixed fluid shell. Because our neutrally-stratified models agree at first order with comparable models that include convection in addition to a laterally-varying CMB heat flux, we argue that our laterally-driven Boussinesq dynamos contain the basic features of more complex models and provide a basic guide for understanding them. We find that strong boundary-modulated flows do not necessitate the cessation of dynamo action. Furthermore, our *Y*10 model suggests that boundary-modulated flows are unlikely to generate more than an order of magnitude hemispherical variation in a planet's surface field. The *Y*11, *Y*20 and *Y*22 Regime III dynamo models all produce equatorially symmetric fields, whereas the *Y*10 model produces a strongly anti-symmetric field. Further, the *Y*11 and *Y*22 models generate strong magnetic flux patches that spatially correlate with strong lateral gradients of outward CMB heat flow, whereas the surface magnetic fields in the *Y*10 and *Y*20 cases cluster mainly within the inner core tangent cylinder.

Acknowledgements

The authors thank David Gubbins and an anonymous referee, as well as Uli Christensen and Sabine Stanley, for their helpful comments. JMA thanks the NSF Geophysics Program (award #EAR-0944312) and NASA's Planetary Atmospheres Program (award #NNX09AB61G) for research support. JA acknowledges support from program PNP/SEDI-TPS of French Institut National des Sciences de l'Univers (INSU). Numerical computations were carried out at S-CAPAD, IPGP.

References

Aubert, J., 2005. Steady zonal flows in spherical shell dynamos. J. Fluid Mech. 542, 53–67.
Aubert, J., Amit, H., Hulot, G., 2007. Detecting thermal boundary control in surface ows from numerical dynamos. Phys. Earth Planet. Inter. 160, 143–156.
Aubert, J., Aurnou, J.M., Wicht, J., 2008. The magnetic structure of convection-driven numerical dynamos. Geophys. J. Int. 172, 945–956.
Aubert, J., Amit, H., Hulot, G., Olson, P.L., 2008. Thermochemical flows couple the Earths inner core growth to mantle heterogeneity. Nature 454, 758–761.
Aubert, J., Labrosse, S., Poitou, C., 2009. Modelling the palaeo-evolution of the geodynamo. Geophys. J. Int. 179, 1414–1428.
Aurnou, J.M., Andreadis, S., Zhu, L., Olson, P.L., 2003. Experiments on convection in Earths core tangent cylinder. Earth Planet. Sci. Lett. 212, 119–134.
Bland, M.T., Showman, A.P., Tobie, G., 2008. The production of Ganymede's magnetic field. Icarus 198, 384–399.
Brachfeld, S.A., Hammer, J., 2006. Rock-magnetic and remanence properties of synthetic Fe-rich basalts: implications for Mars crustal anomalies. Earth Planet. Sci. Lett. 248, 599–617.
Busse, F.H., Simitev, R.D., 2006. Parameter dependences of convection-driven dynamos in rotating spherical fluid shells. Geophys. Astrophys. Fluid Dyn. 100, 341–361.
Cébron, D., Maubert, P., Le Bars, M., 2010. Tidal instability in a rotating and differentially heated ellipsoidal shell. Geophys. J. Int. 182, 1311–1318.
Christensen, U.R., 2006. A deep dynamo generating Mercurys magnetic field. Nature 444, 1056–1058.
Christensen, U.R., Aubert, J., 2006. Scaling properties of convection-driven dynamos in rotating spherical shells and application to planetary magnetic elds. Geophys. J. Int. 117, 97–114.
Courtillot, V., Olson, P.L., 2007. Mantle plumes link magnetic superchrons to phanerozoic mass depletion events. Earth Planet. Sci. Lett. 260, 495–504.
Davies, C.J., Gubbins, D., Jimack, P.K., 2009. Convection in a rapidly rotating spherical shell with an imposed laterally varying thermal boundary condition. J. Fluid Mech. 641, 335–358.
Dobbs-Dixon, I., Lin, D.N.C., 2008. Atmospheric dynamics of short-period extrasolar gas giant planets. I. Dependence of nightside temperature on opacity. Astrophys. J. 673, 513–525.
Elkins-Tanton, L.T., Zaranek, S.E., Parmentier, E.M., Hess, P.C., 2005. Early magnetic field and magmatic activity on Mars from magma ocean cumulate overturn. Earth Planet. Sci. Lett. 236, 1–12.
Gibbons, S.J., Gubbins, D., 2000. Convection in the Earth's core driven by lateral variations in the core–mantle boundary heat flux. Geophys. J. Int. 142, 631–642.
Gibbons, S.J., Gubbins, D., Zhang, K., 2007. Convection in rotating spherical fluid shells with inhomogeneous heat flux at the outer boundary. Geophys. Astrophys. Fluid Dyn. 101, 347–370.
Glatzmaier, G.A., Coe, R.S., Hongre, L., Roberts, P.H., 1999. The role of the Earths mantle in controlling the frequency of geomagnetic reversals. Nature 401, 885–890.
Gonnermann, H.M., Jellinek, A.M., Richards, M.A., Manga, M., 2004. Modulation of mantle plumes and heat flow at the core mantle boundary by plate-scale flow: results from laboratory experiments. Earth Planet. Sci. Lett. 226, 53–67.
Grote, E., Busse, F.H., 2000. Hemispherical dynamos generated by convection in rotating spherical shells. Phys. Rev. E 62, 4457–4459.
Gubbins, D., Roberts, P.H., 1987. Magnetohydrodynamics of the Earth's core. In: Jacobs, J.A. (Ed.), Geomagnetism, 2. Academic Press, London, pp. 1–183.
Gubbins, D., Kelly, P., 1993. Persistent patterns in the geomagnetic field over the past 2.5 Myr. Nature 365, 829–832.
Gubbins, D., Willis, A.P., Sreenivasan, B., 2007. Correlation of Earths magnetic eld with lower mantle thermal and seismic structure. Phys. Earth Planet. Inter. 162, 256–260.
Gubbins, D., Sreenivasan, B., Mound, J., Rost, S., 2011. Melting of Earth's inner core. Nature 473, 361–363.
Harder, H., 1998. Phase transitions and the three-dimensional planform of thermal convection in the Martian mantle. J. Geophys. Res. 103, 16775–16797.
Holme, R., Ingersoll, A.P., 1994. Baroclinic instability in the interiors of the giant planets: a cooling history of Uranus? Icarus 110, 340–356.
Johnson, C.L., Constable, C.G., Tauxe, L., 2003. Mapping long-term changes in Earth's magnetic field. Science 300, 2044–2045.
Kerswell, R.R., Malkus, W.V.R., 1998. Tidal instability as the source of Io's magnetic signature. Geophys. Res. Lett. 25, 603–606.
Khurana, K., Jie, X., Kivelson, M.G., Nimmo, F., Schubert, G., Russell, C.T., 2011. Evidence of a Global Magma Ocean in Ios Interior. Science, 10.1126/science.1201425.
King, E.M., Soderlund, K.M., Christensen, U.R., Wicht, J., Aurnou, J.M., 2010. Convective heat transfer in planetary dynamo models. Geochem. Geophys. Geosys. 11, Q06016.
King, S., 2008. Pattern of lobate scarps on Mercurys surface reproduced by a model of mantle convection. Nature Geosci. 1, 229–232.

Lister, J.R., 2003. Expressions for the dissipation driven by convection in the Earth's core. Phys. Earth Planet. Inter. 140, 145–158.
Nimmo, F., 2000. Dike intrusion as a possible cause of linear Martian magnetic anomalies. Geology 28, 391–394.
Nimmo, F., Hart, S.D., Korycansky, D.G., Agnor, C.B., 2008. Implications of an impact origin for the martian hemispheric dichotomy. Nature 453, 1220–1223.
Olson, P.L., Christensen, U.R., Glatzmaier, G.A., 1999. Numerical modeling of the geodynamo: mechanisms of field generation and equilibration. J. Geophys. Res. 104, 10383–10404.
Olson, P.L., Christensen, U.R., 2002. The time-averaged magnetic eld in numerical dynamos with non-uniform boundary heat ow. Geophys. J. Int. 151, 809–823.
Purucker, M., Ravat, D., Frey, H., Voorhies, C., Sabaka, T., Acuna, M., 2000. An altitude-normalized magnetic map of Mars and its interpretation. Geophys. Res. Lett. 27, 2449–2452.
Roberts, J.H., Lillis, R.J., Manga, M., 2009. Giant impacts and the cessation of the Martian dynamo. J. Geophys. Res. 114, E04009.
Sarson, G.R., 2003. Kinematic dynamos driven by thermal-wind flows. Proc. R. Soc. Lond. A 459, 1241–1259.
Segatz, M., Spohn, T., Ross, M.N., Schubert, G., 1988. Tidal dissipation, surface heat flow, and figure of viscoelastic models of Io. Icarus 75, 187–206.
Sreenivasan, B., 2009. On dynamo action produced by boundary thermal coupling. Phys. Earth Planet. Inter. 177, 130–138.
Stanley, S., Elkins-Tanton, L., Zuber, M.T., Parmentier, E.M., 2008. Mars' paleomagnetic field as the result of a single-hemisphere dynamo. Science 321, 1822–1825.
Stegman, D.R., Jellinek, A.M., Zatman, S.A., Baumgardner, J.R., Richards, M.A., 2003. An early lunar core dynamo driven by thermochemical mantle convection. Nature 421, 143–146.
Sumita, I., Olson, P.L., 2002. Rotating thermal convection experiments in a hemispherical shell with heterogeneous boundary heat flux: implications for the Earths core. J. Geophys. Res. 107, 10.1029/2001JB000548.
Teed, R.J., Jones, C.A., Hollerbach, R., 2010. Rapidly rotating plane layer convection with zonal flow. Geophys. Astrophys. Fluid Dyn. 104, 457–480.
Tackley, P.J., Schubert, G., Glatzmaier, G.A., Schenk, P., Ratcliff, J.T., Matas, J.-P., 2001. Three-dimensional simulations of mantle convection in Io. Icarus 149, 79–93.
Takahashi, F., Tsunakawa, H., Matsushima, M., Mochizuki, N., Honkura, Y., 2008. Effects of thermally heterogeneous structure in the lowermost mantle on the geomagnetic field strength. Earth Planet. Sci. Lett. 272, 738–746.
Torsvik, T.H., Smethurst, M.A., Burke, K., Steinberger, B., 2006. Large igneous provinces generated from the margins of the large low-velocity provinces in the deep mantle. Geophys. J. Int. 167, 1447–1460.
Vallis, G.K., 2006. Atmospheric and Oceanic Fluid Dynamics: Fundamentals and Large-scale Circulation. Cambridge University Press, Cambridge, p. 745.
Wicht, J., 2002. Inner-core conductivity in numerical dynamo simulations. Phys. Earth Planet. Inter. 132, 281–302.
Wicht, J., Tilgner, A., 2010. Theory and modeling of planetary dynamos. Space Sci. Rev. 152, 501–542.
Willis, A.P., Sreenivasan, B., Gubbins, D., 2007. Thermal core mantle interaction: exploring regimes for locked dynamo action. Phys. Earth Planet. Inter. 165, 83–92.
Zhang, K., Gubbins, D., 1992. On convection in the earths core driven by lateral temperature variations in the lower mantle. Geophys. J. Int. 108, 247–255.
Zhang, K., Gubbins, D., 1993. Convection in a rotating spherical fluid shell with an inhomogeneous temperature boundary condition at infinite Prandtl number. J. Fluid Mech. 250, 209–232.
Zhang, K., Gubbins, D., 1996. Convection in a rotating spherical fluid shell with an inhomogeneous temperature boundary condition at finite Prandtl number. Phys. Fluids 8, 1141–1148.
Zhong, S., Roberts, J.H., 2006. Degree-1 convection in the martian mantle and the origin of the hemispheric dichotomy. J. Geophys. Res. 111. doi:10.1029/2005JE002668.